

# A Submillimeter Array Survey of Protoplanetary Disks in the Orion Nebula Cluster

Rita K. Mann<sup>1,2</sup>

and

Jonathan P. Williams<sup>2</sup>

rita.mann@nrc-cnrc.gc.ca, jpw@ifa.hawaii.edu

## ABSTRACT

We present the full results of our 3-year long Submillimeter Array survey of protoplanetary disks in the Orion Nebula Cluster. We imaged 23 fields at  $880\ \mu\text{m}$  and 2 fields at  $1330\ \mu\text{m}$ , covering an area of  $\sim 6.5\ \text{arcmin}^2$  and containing 67 disks. We detected 42 disks with fluxes between 6-135 mJy and at rms noise levels between 0.6 to 5.3 mJy beam<sup>-1</sup>. Thermal dust emission above any free-free component was measured in 40 of the 42 detections, and the inferred disk masses range from  $0.003 - 0.07\ M_{\odot}$ . We find that disks located within 0.3 pc of  $\theta^1\text{ Ori C}$  have a truncated mass distribution, while disks located beyond 0.3 pc have masses more comparable to those found in low-mass star forming regions. The disk mass distribution in Orion has a distance dependence, with a derived relationship  $\max(M_{\text{disk}}) = 0.046 M_{\odot} (d/0.3\text{pc})^{0.33}$  for the maximum disk masses. We found evidence of grain growth in disk 197-427, the only disk detected at both  $880\ \mu\text{m}$  and  $1330\ \mu\text{m}$  with the SMA. Despite the rapid erosion of the outer parts of the Orion disks by photoevaporation, the potential for planet formation remains high in this massive star forming region, with  $\approx 18\%$  of the surveyed disks having masses  $\geq 0.01\ M_{\odot}$  within 60 AU.

*Subject headings:* circumstellar matter — planetary systems: protoplanetary disks — solar system: formation — stars: pre-main sequence

---

<sup>1</sup>National Research Council Canada, Herzberg Institute of Astrophysics, 5071 West Saanich Road, Victoria, British Columbia, Canada V9E 2E7

<sup>2</sup>Institute for Astronomy, University of Hawaii, 2680 Woodlawn Drive, Honolulu, HI 96822

## 1. Introduction

Observations of the circumstellar disks that accompany young stars provide important constraints on the planet formation process. Their fundamental properties, like mass and size, play a significant role in the potential to form planets, and may determine the types of planets that can form. Our current understanding of disk properties has been expanded through extensive millimeter wavelength studies of the nearest, young, low-mass star forming regions, Taurus-Auriga and  $\rho$ Ophiuchus (e.g., Beckwith et al. 1990; Osterloh & Beckwith 1995; Andre & Montmerle 1994; Andrews & Williams 2005, 2007a). The stars in these low-mass star forming regions evolve in relative isolation where only internal processes affect their disk properties and evolution, and their observations represent an important starting point to understanding single star and disk evolution.

The vast majority of stars in the galaxy, however, were not created in regions like Taurus-Auriga or  $\rho$ Ophiuchus, but in rich clusters that contain massive ( $> 8 M_{\odot}$ ) O-type stars. Surveys of low-mass star formation show that 70-90% of stars within 2 kpc of the Sun formed in rich, embedded clusters,  $\sim 75\%$  of which currently contain massive stars (Lada & Lada 2003). Moreover, the mass distribution of molecular clouds is weighted toward the most massive clouds, which are more likely to form rich clusters containing O-type stars (see Evans 1999). There is even clear evidence that our Sun was born in a massive star forming environment. Studies of primitive meteorites have revealed they contain the decay products of  $^{60}\text{Fe}$ , which can only be produced by a supernova, unambiguously placing the Sun’s formation near at least one massive star (Tachibana et al. 2006; Krot et al. 2005; Gaidos et al. 2009).

In rich clusters, external influences on disk evolution become important and they can threaten the development and persistence of protoplanetary disks. The high density of stars can lead to enhanced probabilities of dynamical interactions (Bonnell et al. 2003), while UV radiation from O-type stars can evaporate the disk material (Johnstone et al. 1998). Such is the case in the Orion Nebula, which is the nearest, young, massive star forming region. Hundreds of young stars lie within the central 0.2 pc of the Orion Nebula Cluster (ONC) (Hillenbrand 1997), where the single,  $\sim 1$  Myr old,  $45 M_{\odot}$ , O6-type star,  $\theta^1$  Ori C, dominates the radiation field of the region. Normally, protostars like those in Orion would be deeply embedded leaving them highly obscured throughout their formation. But the massive OB-stars of the Trapezium cluster, located at the heart of the Orion Nebula, have carved out a cavity with their radiation, clearing out the molecular cloud material along our line of sight, leaving a “blister HII” region. The fortuitous viewing geometry leaves the stars only slightly extincted ( $A_v < 2.5$  mag; Hillenbrand 1997), allowing observational access into the molecular cloud at optical to infrared wavelengths.

The young stars in Orion were initially identified at optical and radio wavelengths as ionized envelopes surrounding neutral condensations (Laques & Vidal 1979; Moran et al. 1982; Garay et al. 1987) and were later hypothesized to be circumstellar disks surrounding young stars by Churchwell et al. (1987) through centimeter wavelength VLA observations. Churchwell et al. (1987) measured high mass-loss rates of  $\dot{M} \sim 10^{-6} - 10^{-7} M_{\odot} \text{ yr}^{-1}$ , which they reasoned implied a large reservoir of neutral circumstellar material that would render the young stars invisible at optical and infrared wavelengths unless it was distributed in a disk-like geometry. Hubble Space Telescope (HST) images of the region spectacularly confirmed the disk hypothesis by imaging the externally illuminated objects and revealing they were circumstellar disks of dust and gas that are evaporating under the intense UV flux from the most luminous star of the cluster,  $\theta^1$  Ori C (O’de11 et al. 1993; O’de11 & Wen 1994).

The young objects were named “proplyds” by O’de11 et al. (1993), an acronym for PROtoPLANetarY DiskS, because they appeared remarkably different from isolated disk systems observed in low-mass star forming regions. To date, nearly 200 proplyds have been discovered in Orion through high resolution optical and near-IR observations with HST (O’de11 & Wong 1996; Bally et al. 1998a, 2000; Smith et al. 2005; Ricci et al. 2008). Most of the proplyds appear strongly ionized; they are surrounded by cometary shaped ionized gas cocoons, with bright heads facing  $\theta^1$  Ori C, and tails facing away (McCullough et al. 1995; Bally et al. 1998a). A small percentage of the disks are dark silhouettes, seen in extinction against the bright background nebula (see McCaughrean & O’de11 1996), or embedded silhouettes, projected against the glowing light from their own ionized cocoons. The pure dark silhouettes show no evidence of being photoevaporated and are likely not in the center of the Trapezium Cluster but only appear so in projection.

Given the mass-loss rates of the disks, ( $\dot{M} \sim 10^{-6} - 10^{-7} M_{\odot} \text{ yr}^{-1}$ ), which are high enough to remove a MMSN ( $0.01 M_{\odot}$ ) in  $\leq 10^5 \text{ yr}$  (Churchwell et al. 1987; Henney & O’De11 1999), it was questioned whether enough raw material could remain in the disks to allow planets to form. However, there is a critical radius surrounding each star,  $r_g$ , within which the gravitational potential of the star confines material to the system for longer than planet formation timescales (Johnstone et al. 1998; Adams et al. 2004). While it takes 0.1 to 1.0 Myrs to remove the outer disk beyond  $r_g \sim \frac{GM_{\star}}{a^2}$ , where  $a$  is the sound speed in the gas, an additional 10-30 Myrs is required to erode the disk down to 20 AU scales, into the planet forming zones (Adams et al. 2004; Clarke 2007). If enough mass exists within  $r_g$  of the Orion proplyds, then planet formation remains a possibility despite UV photoevaporation.

Although extensive observations have been made of the Orion proplyds at optical, infrared and radio wavelengths, none of these observations were able to yield disk masses. The disks are purely absorbing at optical and near-infrared wavelengths, and therefore, obser-

vations were only capable of placing lower limits on their column densities and masses, of  $5 \times 10^{-4} M_{\odot} = 0.5 M_{Jup}$  (McCaughrean et al. 1998). At radio wavelengths, the emission from the proplyds is dominated by free-free emission originating in the ionized gas cocoons, which swamps the weaker dust-disk emission. In most cases, disk masses can only be estimated from measurements of optically thin dust continuum emission at millimeter wavelengths. The millimeter spectral energy distribution (SED) of a disk originates from dust located in the cool, disk midplane. While the infrared observations are sensitive to only  $\sim 1\%$  of the total dust mass (or dust volume), the millimeter observations are sensitive to dust located out to hundreds of AU, where the majority ( $>90\%$ ) of the mass lies. Low column densities at these radii make the emission optically thin, leading the disk luminosity to be proportional to the sum of emission from all dust grains. This yields a direct relationship between submillimeter flux density  $F_{\nu}$  and disk mass  $M_d$  (Beckwith et al. 1990), providing one of the best ways for masses to be measured. Disk masses are often compared to a reference called the Minimum Mass Solar Nebula (MMSN= $0.01 M_{\odot}$ ), which represents a lower limit on the amount of gas and dust that was present in the primordial Solar System disk when the planets began formation (Weidenschilling 1977).

Since their discovery by HST imaging, the Orion proplyds have been surveyed by many millimeter wavelength interferometers in an attempt to measure their masses and infer their potential to form planets (BIMA at 3.5-mm, Mundy et al. 1995; OVRO at 1.3-mm, Bally et al. 1998b; OVRO at 3-mm, Eisner & Carpenter 2006; CARMA and SMA at 1.3-mm; Eisner et al. 2008) but few disks were detected due to the limited sensitivity to dust emission at these long wavelengths. Even at millimeter wavelengths, the substantial levels of free-free emission swamps the thermal dust emission from the disks, making mass estimates difficult to impossible. The dust emission increases sharply with frequency, having a dependence of  $F_{\nu} \propto \nu^2$ , and so the first successful detections of dust emission from the Orion proplyds came at *sub*-millimeter wavelengths,  $880 \mu\text{m}$  observations with the Submillimeter Array (SMA) (Williams et al. 2005). Four proplyds were detected by Williams et al. (2005) having disk masses of 0.013-0.028  $M_{\odot}$ , exceeding the MMSN, and showed the capacity for Orion disks to be truly protoplanetary.

Building on the success of the pilot study observations by Williams et al. (2005) we carried out an SMA survey at  $880 \mu\text{m}$  and  $1330 \mu\text{m}$  of protoplanetary disks in the Orion Nebula Cluster from late 2006 to early 2010. The goal of the survey was to measure the disk mass distribution in a rich cluster in order to study the impact of massive stars on disk evolution. In this paper, we present the results of our complete survey, with observations taken at  $880 \mu\text{m}$  and  $1330 \mu\text{m}$ , covering 23 SMA fields and 67 proplyds. We targeted only HST-identified circumstellar disks, as there is no ambiguity about the geometry of their dust distributions. Two main results from the survey have been published to date, showing the

inner 0.2 pc of the Orion Nebula lacks the largest and most massive disks observed in low-mass star forming regions (Mann & Williams 2009a), while the outer regions, beyond 1 pc from  $\theta^1$  Ori C, do not (Mann & Williams 2009b). Here, we present new SMA observations taken of disks located at intermediate distances ( $d=0.2$ -1 pc) from  $\theta^1$  Ori C, to study the disk mass dependence on distance in the Orion Nebula Cluster. We describe the observations and data reduction methods in §2 and present the calculation of disk masses in §3. We examine the dependence of disk mass on size and location within the cluster and also discuss the results and implications for planet formation in rich clusters in §4.

## 2. Observations

Submillimeter interferometric observations of 23 fields containing 67 proplyds were conducted with the Submillimeter Array (SMA; Ho et al. 2004) between 2006 Dec 27 and 2010 Jan 29 on Mauna Kea. We used the compact and extended array configurations of the SMA; see Table 1 for a journal of the observations. The compact configuration was chosen for observations prior to 2009, to provide the best phase stability, and maintain sufficient resolution ( $\sim 2.5''$  at  $880\ \mu\text{m}$ ) to distinguish individual proplyds. Data taken in 2009-2010 were obtained using the extended configuration of the SMA, which takes advantage of improvements to the array, particularly bandwidth doubling.

The phase centers of the observations (Table 1, Figure 1) were chosen to simultaneously maximize the number of proplyds imaged while minimizing contamination from the bright, nonuniform background (see Section 3.2). Double sideband receivers were tuned to local oscillator (LO) frequencies of 340.175 GHz, 350.175 GHz or 224.170 GHz (882, 857 or 1330  $\mu\text{m}$ , respectively: see Table 1). For observations taken prior to August 2009, each sideband provided 2 GHz of bandwidth, separated by  $\pm 5$  GHz from the LO frequency. Subsequent observations benefited from an increased 4 GHz of bandwidth per sideband, separated by  $\pm 6$  GHz from the LO frequency. Each observation listed in Table 1 represents a full 8 hour track, except the last 6 fields (18-23), which were shared between pairs of fields because of the increased bandwidth. For the initial fields, we simultaneously observed the CO(3–2) and HCN(4–3) transitions by using an LO of 350 GHz. When it became clear that the line emission from the disk could not be distinguished from the extended molecular cloud emission, observations were switched to slightly lower frequencies (340 GHz) where both the atmosphere and receiver performance improves (see Table 1). CO(3–2), HCN(4–3), CO(2–1) and  $^{13}\text{CO}(2-1)$  were all detected but maps show they were indistinguishable from the cloud background and we do not discuss them further.

Weather conditions for all observations were good, with  $< 2$  mm precipitable water

vapor, or  $\tau(225 \text{ GHz}) < 0.1$  for  $880 \mu\text{m}$  observations and  $< 5 \text{ mm}$ , or  $\tau(225 \text{ GHz}) < 0.24$  for  $1330 \mu\text{m}$  observations. The atmosphere was very stable during the nights and system temperatures ranged from 100–400 K. The total rms noise levels after calibration ranged from 0.6 to 6.0 mJy. Table 1 summarizes the relevant observational information.

The raw visibilities for each night were calibrated and edited using the MIR software package. Amplitude and phase calibration were performed through observations of the bright quasars J0423-013 and J0530+135. The compact array observations were interleaved between 20-minute target observations of the proplyds, and 5-minute observations of each of the two quasars. We shortened the target integration to 15-minutes for the extended array observations to increase our monitoring of the quasars. Passband calibration was conducted with one of 3C454.3, 3C279, or 3C273. The flux scale was derived using measurements of Titan or Uranus as primary flux calibrators; we used the values derived by Mark Gurwell, available at <http://sma1.sma.hawaii.edu/callist/callist.html>. The flux scale is estimated to be accurate to  $\sim 15\%$ .

The calibrated visibilities were weighted by system temperature and inverted, then cleaned to generate the synthesized continuum maps shown in Figures 2 & 3 using MIRIAD (Sault et al. 1995). All line transitions were edited out of the observations before producing the final images. The maps were created after eliminating  $uv$ -spacings shorter than  $27 \text{ k}\lambda$  (physical baselines shorter than 23-m) to filter out uniform extended emission corresponding to size scales larger than  $7.5''$ . The size scale was chosen to preserve compact emission from the disks, while minimizing contamination from bright, extended cloud background. Simulations of the background (see Section 3.2) confirmed that the  $27 \text{ k}\lambda$  cutoff would resolve out the majority of extended emission and reduce the rms noise levels by factors of 2 to 3.

### 3. Results

The 23 SMA fields included a total of 67 HST-identified disks from the catalogs of O’dell & Wong (1996), Bally et al. (2000), Smith et al. (2005), and Ricci et al. (2008) and are shown in Figure 1. Continuum flux densities,  $F_{\text{obs}}$ , were determined for each source by summing the emission within a  $2\sigma$  contour, and correcting for primary beam attenuation. The rms noise levels were determined using as much of the emission-free regions within the SMA primary beam. In total, we detected 42 of the 67 surveyed disks with signal-to-noise ratio’s  $\geq 3$ .

Before disk masses can be calculated, we need to separate the flux contributions from thermal dust emission from the disks,  $F_{\text{dust}}$ , the free-free emission from the ionized cocoons,

$F_{\text{ff}}$ , and the background molecular cloud emission,  $F_{\text{bg}}$ :

$$F_{\text{obs}} = F_{\text{dust}} + F_{\text{ff}} + F_{\text{bg}} \quad (1)$$

The following sections describe how  $F_{\text{ff}}$ ,  $F_{\text{bg}}$ , and  $M_{\text{disk}}$  were determined.

### 3.1. Free-Free Emission, $F_{\text{ff}}$

The radio-submillimeter SEDs for the 42 disks detected at  $\geq 3\sigma$  at  $880\mu\text{m}$  with the SMA are shown in Figures 4 and 5. We used VLA observations at centimeter wavelengths from Garay et al. (1987); Felli et al. (1993); Zapata et al. (2004), and BIMA, OVRO, CARMA and SMA upper limits and detections at millimeter wavelengths (Mundy et al. 1995; Bally et al. 1998b; Eisner & Carpenter 2006; Eisner et al. 2008) to define the free-free spectrum and then extrapolated it into the submillimeter regime. Fits to the free-free emission ( $F_{\nu} \propto \nu^{-0.1}$ ) and dust emission ( $F_{\nu} \propto \nu^2$ ) are overlaid on the SEDs to show their relative contributions and contrasting spectral dependences. The long wavelength, 6 cm to 1.3 mm, data show a flat spectral dependence consistent with optically thin emission,  $\nu^{0.1}$ , but with a range, highlighted by the grey scale, which we attribute to variability (Felli et al. 1993; Zapata et al. 2004). We avoided observations taken at wavelengths longer than 6 cm (5 GHz) in this analysis, in order to avoid the turnover frequency, where the free-free emission becomes optically thick and no longer follows a  $\nu^{-0.1}$  dependence. These SEDs show how substantial the free-free emission towards the Orion proplyds is, swamping the thermal dust emission from centimeter to millimeter wavelengths, and demonstrating why higher frequency, submillimeter observations are necessary to detect dust emission from these disks.

The disks within fields 12 through 23 were not detected in previous surveys at radio to millimeter wavelengths and, with the exception of disk 072-135, none of the disks show signs of photoevaporation through their HST images, therefore their flux contribution from ionized gas emission is expected to be negligible at submillimeter wavelengths ( $F_{\text{ff}} \ll 1$  mJy).  $F_{\text{ff}}$  is listed in Table 2, and is the maximum level of free-free radiation extrapolated to the observing frequency. After subtracting off the free-free contribution to the proplyd fluxes, 40 of the 42 detected proplyds had dust emission in excess of the ionized gas emission. The SMA emission detected towards two proplyds, 168-326NS and 180-331, is consistent with free-free emission and these are therefore listed in Table 3 instead of Table 2.

### 3.2. Background molecular cloud emission $F_{\text{bg}}$

The Orion proplyds lie within a blister HII region which sits in front of a giant molecular cloud. The submillimeter emission from the cloud was mapped with the SCUBA camera on the James Clerk Maxwell Telescope (JCMT) by Johnstone & Bally (1999); see background of Figure 1. The unfiltered background intensity is  $\sim 1\text{-}3$  Jy per  $15''$  SCUBA beam, which corresponds to a flux of  $\sim 10\text{-}30$  mJy per compact array SMA beam, or a contribution of  $\sim 5 - 15 \times 10^{-3} M_{\odot}$  to a typical disk mass. The SMA, however, resolves out much of this emission if it is extended.

To characterize the effects of a strong background on the noise properties of each field, we performed simulations of the interferometric response to the extended cloud emission. The simulations were conducted using the array configurations and  $uv$ -tracks from the observations and applying them to the corresponding positions in the SCUBA map. For each field, the SCUBA data were Fourier-transformed and sampled over the observational  $uv$ -tracks, inverted and cleaned. Spatially filtered maps of the background were made using  $uv$ -spacings  $\geq 27$  k $\lambda$ , to filter out the uniform extended emission on angular scales  $\geq 7.5''$ , exactly as used to produce the final SMA maps described in §2. The flux contribution from the background emission,  $F_{\text{bg}}$ , was determined by summing the emission within an SMA beam sized aperture placed at the position of the individual proplyd within the simulated maps. The values of  $F_{\text{bg}}$  are listed in Table 2. Using the clump mass spectrum in Orion (Johnstone et al. 2001, 2006; Johnstone & Bally 2006), we estimate the probability of background contamination from small clumps ( $7.5''\text{-}15''$ ) not detectable by SCUBA observations to be negligible, with  $\approx 10^{-3}$  detectable clumps per  $35''$  SMA primary beam.

### 3.3. Disk Masses

The submillimeter continuum emission is produced by dust grains in the disk, which absorb stellar UV and optical photons, and re-emit them at longer, infrared to millimeter, wavelengths. Submillimeter wavelength emission is sensitive to dust throughout the disk, where the majority ( $>90\%$ ) of the disk mass lies. Low column densities beyond  $\sim 20$  AU imply that the emission is mostly optically thin and the submillimeter fluxes depend directly on the total mass present in the disk:

$$M_{\text{disk}} = \frac{d^2 F_{\nu}(T)}{\kappa_{\nu} B_{\nu}(T)}. \quad (2)$$

The largest uncertainty in this calculation of disk masses lies in the value of the dust



mass opacity,  $\kappa_\nu$ , the ratio of effective dust cross section to mass, which depends strongly on the dust grain characteristics (Beckwith et al. 1990).

We determined disk fluxes,  $F_{\text{dust}}$ , according to Equation 1; see Table 2. Disk masses were then calculated for the 40 Orion proplyds detected in significant dust emission using Equation 2. We used a distance to Orion of 400 pc, which is based on recent measurements, including parallax observations of stars in the cluster, (Menten et al. 2007; Sandstrom et al. 2007) and the orbital motion of binaries in the cluster (Kraus et al. 2007, 2009). We used the Beckwith et al. (1990) dust mass opacity,  $\kappa_\nu = 0.1(\nu/1000 \text{ GHz}) \text{ cm}^2\text{g}^{-1}$ , which implicitly assumes a 100:1 gas to dust mass ratio. We used a dust temperature of 20 K, the average for disks in Taurus-Auriga and  $\rho$  Ophiuchus (Andrews & Williams 2005, 2007a); see also Williams et al. (2005). The final disk masses and upper limits for the non-detections are listed in Tables 2 and 3.

The conversion of flux to disk mass is conventional and was chosen for the simplicity of comparison with other continuum studies, for example, in Taurus and  $\rho$  Ophiuchus (Andrews & Williams 2005, 2007a). Longer wavelength observations of Orion disks without substantial free-free emission show grain growth to beyond millimeter sizes (Ricci et al. 2010b, in press), as is also seen in Taurus and  $\rho$  Ophiuchus. The effect lowers the overall dust opacity,  $\kappa_\nu$ . Less direct evidence based on disk accretion rates and ages also suggest that disk masses may, in general, be underestimated by between a factor of 4-8 (Hartmann et al. 1998; Andrews & Williams 2007a). The disk masses derived here should be considered lower limits but this is somewhat mitigated by their comparison to a low estimate of the MMSN.

The mass sensitivity of this survey depends on many factors, including the varying levels of free-free and background emission contributing to the observed fluxes, as well as the location of the proplyds within each field. We, therefore, derived our completeness level by performing Monte Carlo simulations to determine the fraction of sources that could be detected at  $\geq 3\sigma$  as a function of mass, depending on the above-mentioned characteristics. The results reveal that our survey is 100% complete for disk masses  $M_d \geq 0.0084 M_\odot$  and 50% complete for  $M_d \geq 0.003 M_\odot$  (see also Mann & Williams 2009a).

### 3.4. 1330 $\mu\text{m}$ observations

Although most proplyds appear to be strongly ionized, there are a small number of silhouette disks which show no evidence of photoevaporation through their HST images and have negligible free-free emission levels at radio wavelengths. For these silhouette disks, we attempted to detect dust emission at a slightly longer wavelength of 1330  $\mu\text{m}$ . The detection

of dust at more than one wavelength, on similar baselines, allows us to study the spectral behavior of the Orion disk emission and constrain their dust properties by comparing them with disks in Taurus and  $\rho$ Ophiuchus.

In the Rayleigh-Jeans (R-J) limit ( $h\nu \ll kT$ ), the Planck blackbody function has the dependence  $B \propto \nu^2$ , resulting in the submillimeter flux emission behaving as a simple power law in frequency,  $F_\nu \propto \nu^{2+\beta}$ . The power-law index,  $\beta$ , is a function of the dust grain size, shape and composition. If a uniform shape and composition are assumed, knowledge of  $\beta$  can constrain the dust size distribution and expose whether the growth of particles has begun in the disk. The determination of  $\beta$  can be complicated if there is significant deviation from the R-J criterion or if there is a contribution of optically thick emission to the disk flux (Beckwith et al. 1990). For these reasons, we empirically describe the submillimeter continuum emission as  $F_\nu \propto \nu^\alpha$ , with  $\alpha$  related to  $\beta$ , but with a minor correction (typically  $\Delta\beta \sim$  a few tenths), for optically thick emission from the inner disk (see Beckwith et al. 1990; Beckwith & Sargent 1991).

We observed two fields at  $1330\mu\text{m}$ , which were centered on silhouette disks 182-413 and 114-426 (Fields 2 and 3), neither of which were detected (see Figure 7 for observations of disk 114-426). The proplyd 197-427, which lies in the primary beam of Field 2, was detected at  $1330\mu\text{m}$ , with a primary beam corrected flux of 17.4 mJy (see Figure 6, Table 4). Disk 197-427 is the only proplyd in Orion detected at both  $880\mu\text{m}$  and  $1330\mu\text{m}$  with our SMA observations. The slope of its submillimeter emission, determined from a ratio of its  $1330\mu\text{m}$ ,  $880\mu\text{m}$  fluxes, is  $\alpha = 2.8 \pm 0.1$ . This slope is intermediate between that found for a typical Class II disk in Taurus-Auriga or  $\rho$ Ophiuchus with  $\alpha \sim 2$  (Andrews & Williams 2005, 2007a; Rodmann et al. 2006; Ricci et al. 2010), and the ISM, which contains sub- $\mu\text{m}$  sized dust particles and has an  $\alpha \sim 4$  (Pollack et al. 1994). In both Taurus and  $\rho$ Ophiuchus, and recently, in Orion (see Ricci et al. 2010b, in press), the systematic change observed in the submillimeter slope with disk evolutionary state is most readily interpreted as due to grain growth in the disks to at least millimeter sizes. Therefore, the slope of Orion disk 197-427 suggests dust grain growth may be underway in this disk. Its spectral slope is actually more consistent with a Class I Taurus disk than a Class II disk, which we speculate could be due to photoevaporation of the surrounding circumstellar envelope, leading to the premature emergence of a Class II disk in Orion.

Disks 182-413, 174-414 and 183-419 were detected at  $880\mu\text{m}$ , but not at  $1330\mu\text{m}$ , so we can place constraints on their spectral slopes using their  $3\sigma$  flux upper limits at  $1330\mu\text{m}$ . Fluxes, upper limits and  $\alpha$  values for these disks are listed in Table 4. The estimated spectral slopes for Orion disks lie within with the range found for disks in Taurus or  $\rho$ Ophiuchus, which show  $\alpha=1-4$  (Andrews & Williams 2005, 2007a; Rodmann et al. 2006;

Ricci et al. 2010).

### 3.5. Near-Infrared Excess Stars

Near-infrared emission in excess of stellar photospheric emission is often interpreted to be due to the presence of circumstellar disks around young stars. Vicente & Alves (2005) noted that HST-observations were only able to identify disks around  $\sim 50\%$  of the IR-excess stars in the Orion Nebula Cluster and suggested that the remaining disks were too small,  $< 0.15'' \approx 60$  AU in extent, to be resolved by HST imaging. In addition to the HST-identified proplyds which were the primary targets of our survey, there were also 43 near-IR sources lying within the SMA fields. With the exception of one source, ID=253 from Hillenbrand & Carpenter (2000), which was detected at  $\sim 3\sigma$  in Field 1, only IR-excess stars with HST-identified counterparts were detected by the SMA. The vast majority of the infrared-only disks were not detected by our observations, implying they are not only small in size, but also low in mass.

## 4. Discussion

### 4.1. Non-Detection of the Giant Silhouette Disk 114-426

Surprisingly, the most prominent Orion disk, 114-426, an 1100 AU silhouette disk seen nearly edge-on in HST images, was not detected by the SMA at either  $880\ \mu\text{m}$  or  $1330\ \mu\text{m}$  (see Figure 7). The non-detection places a  $3\sigma$  upper mass limit of  $0.012\ M_{\odot}$  on the disk at  $880\ \mu\text{m}$ , which includes a background flux correction of  $F_{\text{bg}} = -12.8$  mJy (see Table 3). The previous disk mass upper limit based on a  $1330\ \mu\text{m}$  OVRO non-detection (Bally et al. 1998b) is  $< 0.033\ M_{\odot}$ , which we re-calculated using the improved distance to Orion of 400 pc, and the same  $T$ ,  $\kappa_{\nu}$  as our study. By studying the extinction of disk 114-426 at multiple wavelengths, McCaughrean et al. (1998) derived a lower limit on its mass of  $5 \times 10^{-4}\ M_{\odot}$ . Together, these limits impose a disk mass on 114-426 between  $5 \times 10^{-4}$ - $1.2 \times 10^{-2}\ M_{\odot}$  ( $0.5$ - $12M_{\text{Jup}}$ ).

The stringent mass upper limit of  $10^{-2}\ M_{\odot}$  on 114-426 is puzzlingly low considering its large extent. But the non-detection may not be surprising if we consider the background emission toward this source. Our SMA simulations, described in Section 3.2, demonstrated that the ridge of bright background emission that is clearly visible in Figure 1, dominates the noise in the sensitive interferometric observations of the region. Although we deliberately planned many of our observations to avoid the bright ridge, we made an exception for 114-

426. The high contribution from the background emission toward 114-426 is evident in the rms noise levels of both 880  $\mu\text{m}$  and 1330  $\mu\text{m}$  observations, which are higher than for pointings not located near the bright ridge (see Figure 7, Table 1). The estimated background flux within an SMA beam-sized aperture toward 114-426 is  $F_{\text{bg}} = -12.8$  mJy, the largest absolute contribution toward any disk in our entire sample (see Tables 2, 3). Therefore, the substantial noise levels towards disk 114-426 are not likely due to instrumental issues, but due to small scale inhomogeneities in the background emission towards this source. We, therefore, believe that disk 114-426 was not detected by our SMA observations because of its location near the strong, contaminating, background molecular cloud emission in the Orion Nebula.

The lack of millimeter emission detected toward disk 114-426 has also been attributed to the growth of dust particles to large sizes that no longer emit efficiently at these wavelengths (Bally et al. 1998a; Throop et al. 2001). It is well-established that grain growth is a rapid process in protoplanetary disks (e.g., D’Alessio et al. 2001; Wilner et al. 2005; Dullemond & Dominik 2005). However, grain growth must be balanced by collisional fragmentation in order to match observations that reveal disks remain rich in small dust grains for up to several Myrs (Dullemond & Dominik 2005; Birnstiel et al. 2009). It is also difficult to reconcile the grain growth explanation with images of the disk taken at  $\lambda=0.4\text{--}4\mu\text{m}$  (McCaughrean et al. 1998; Throop et al. 2001; Shuping et al. 2003; Ricci et al. 2008), which require a population of  $\mu\text{m}$ -sized particles to generate. Studies of disk extinction as a function of wavelength (McCaughrean et al. 1998; Shuping et al. 2003) have even shown that most dust grains along the disk edges of 114-426 cannot be significantly larger than 4-5 $\mu\text{m}$ . Therefore, the primary reason for the non-detection of disk 114-426 by SMA observations is interference from the strong, background emission toward this source, not grain growth.

## 4.2. Disk Masses and Sizes

Theoretical models of disk photoevaporation predict that the most extended disks should experience the highest mass-loss rates because material at larger radii is more loosely bound to the embedded star and it provides a broader surface area for photoevaporation. Mass-loss occurs in the disks when the sound speed in the gas exceeds the escape velocity:  $c_s = (kT/\mu m_H)^{\frac{1}{2}} \geq v_{\text{esc}} = (GM_\star/R)^{\frac{1}{2}}$ , or for disk radii  $R_{\text{disk}} \gtrsim M_\star/T$ , where  $T$  is the temperature of the UV-heated disk gas and  $M_\star$  is the stellar mass. Escape velocities increase towards smaller radii, requiring the disk gas be heated to higher temperatures,  $T \sim 1/R_{\text{disk}}$ , before mass-loss can occur. Mass-loss rates drop two orders of magnitude, from  $\dot{M} \sim 10^{-7} M_\odot \text{ yr}^{-1}$  for 100 AU disks to  $\sim 10^{-9} M_\odot \text{ yr}^{-1}$  for 20 AU disks (Johnstone et al. 1998; Adams et al. 2004), removing the outer disks ( $> 50\text{--}100\text{AU}$ ) in 0.1-1.0 Myrs, while allowing the gravita-

tionally bound, inner ( $< 50\text{AU}$ ) disks to endure for  $\gtrsim 10\text{ Myrs}$  (Adams et al. 2004; Clarke 2007). The youth of  $\theta^1\text{ Ori C}$  (Hillenbrand 1997) implies a photoionizing age  $< 1\text{ Myr}$ , and we, therefore, expect the outer disks of stars located near the Trapezium Cluster to be stripped away while the inner disks persist.

To investigate the relationship between mass-loss and disk sizes, we plotted our calculated disk masses versus radii for 31 silhouette disks with resolved sizes from HST imaging in Figure 8; disk radii were taken from Vicente & Alves (2005). We did not use the sizes of the unresolved Orion proplyds from Vicente & Alves (2005) in this analysis because they do not have directly measured disk radii. The vertical dashed line in Figure 8 represents the resolution of the HST images,  $0.15'' \approx 60\text{ AU}$  at the distance of Orion. We expect photoevaporating disks to lose mass and grow smaller simultaneously, moving them from the upper right corner of Figure 8 to the bottom left, an effect that is consistent with the observations shown.

The diversity of initial disk properties within this sample obscures a clear-cut signature of the relationship between disk mass and size. For example, if we assume all the disks have similar surface density profiles, with  $\Sigma = \Sigma_0(r/R_0)^{-1}$ , then the disk masses,  $M = 2\pi\Sigma_0 R_0 R$ , depend not only on disk size,  $R$ , but also on the surface density normalization,  $\Sigma_0$ . Disk masses and sizes are further complicated by their dependence on stellar mass, which sets the gravitational radius for how far photoevaporation can erode the disk on planet formation timescales, and on distance from  $\theta^1\text{ Ori C}$ , which also influences the mass-loss rates. Yet, despite the complexity of the relationship, we find evidence of a correlation between disk mass and size. The largest disks tend to be the most massive, and there is a lack of large, low-mass disks. The probability of correlation between disk mass and radius ranges from 95.4%-99.95% ( $2.0\sigma - 3.5\sigma$ ; see Table 5), which were calculated using various censored statistical tests that incorporate the  $3\sigma$  upper limits for the non-detections (Isobe et al. 1986).

Spatially resolved observations of many disks in Taurus-Auriga and  $\rho\text{ Ophiuchus}$  have revealed that the disk surface density profiles quite uniformly follow a  $\Sigma \sim r^{-1}$  dependence within  $\sim 100\text{-}200\text{ AU}$  (Andrews et al. 2009; Andrews & Williams 2007b). We also plot in Figure 8, three diagonal dashed lines, which are comparisons to  $M_{\text{disk}}$  for three normalizations of the surface densities,  $\Sigma_0$ , where  $\Sigma = \Sigma_0(r/R_0)^{-1}$ . The uppermost normalization plotted is the surface density at 5 AU for a MMSN-disk,  $\Sigma_5(\text{MMSN}_{60})$ , which we define here to contain  $0.01 M_\odot$  within  $R_0 = 60\text{ AU}$ :  $\Sigma_5(\text{MMSN}_{60}) = 0.01 M_\odot / 2\pi(60\text{ AU})(5\text{ AU}) = 47.2\text{ g cm}^{-2}$ . The remaining two profiles shown are a factor of  $\sqrt{10}$  and 10 lower. The photoevaporation of disks should shift them to smaller sizes and masses along these surface density scalings. The normalizations plotted reveal that the majority of Orion silhouette disks have low surface densities when compared with the standard, MMSN. We also estimated the normalized disk

surface densities at 5 AU,  $\Sigma_5$ , for the Orion silhouette disks to compare them with Taurus and  $\rho$  Ophiuchus disks (see Figure 9). The histograms of  $\log(\Sigma_5)$ , are shown for Orion on top and Taurus/ $\rho$  Ophiuchus below, with data taken for the latter set from Andrews & Williams (2007b). The Orion distribution shows a broad peak near a surface density of  $\sim 20 \text{ g cm}^{-2}$  at 5 AU. The MMSN surface density at 5 AU is shown by the dashed line in Figure 9. The distributions between the regions are similar, with many disks appearing to have lower surface densities than the standard of reference, MMSN.

### 4.3. Dependence of Disk Mass on Distance from $\theta^1$ Ori C

All theoretical models of protoplanetary disk photoevaporation by O-stars agree in predicting that the most rapid disk erosion occurs for the largest disks located near  $\theta^1$  Ori C (Johnstone et al. 1998; Störzer & Hollenbach 1999; Richling & Yorke 2000; Scally & Clarke 2001; Matsuyama et al. 2003; Adams et al. 2004). In Orion, the incident radiation field from the massive stars can be described by its ratio to the interstellar (Habing) field as  $G_0 = 13,000/d_{pc}^2$  (Parravano et al. 2003). Adams et al. (2004) calculated the gas temperatures of photoevaporating disks under various radiation fields (see their Figure 2) and showed that the disk temperatures scale roughly with the radiation field:  $T \sim G_0^{\frac{1}{2}}$ . Therefore, at increasing distances from the massive stars, UV-heating of the disks declines,  $T \sim 1/d$ , allowing larger and more massive disks (see previous section) to survive photoevaporation:  $R_{disk} \sim 1/T \sim d$ .

In order to examine the dependence of disk mass on location in the cluster, we plotted our calculated Orion disk masses versus their projected distances from  $\theta^1$  Ori C in Figure 10. The most massive disks in the cluster are found at the largest distances from  $\theta^1$  Ori C, while the erosion of the upper end of the mass distribution towards smaller distances is clear from this figure. It is also interesting to note that all of the non-detections lie within 0.3 pc from  $\theta^1$  Ori C. As approximately half of the survey sample were non-detections, we used censored statistical tests to calculate correlation probabilities. Results of the statistical tests support a correlation between Orion disk masses and projected distances from  $\theta^1$  Ori C, with high probabilities that range between 98.74% to 100%; 2.5-4.0  $\sigma$  (see Table 5). We used projected distances because the true distances of the disks from  $\theta^1$  Ori C are unknown. As a consequence, depending on their radial distance from  $\theta^1$  Ori C, the disks could in fact lie at larger distances from the central cluster, which would shift their positions in Figure 10 to the right. However, such an adjustment is not likely to severely alter the trend of increasing maximum disk masses with distance. And in spite of the intrinsic diversity of initial disk properties, which should produce an observable spread in any real correlation, we

find compelling evidence of a dependence between disk mass and distance from an O-star in the cluster.

The most massive disks are the most readily detectable in our SMA survey and are subject to the least observational bias. The maximum disk mass envelope in Orion is traced by the long, dashed line across the top of Figure 10. The trend of increasing maximum disk mass with respect to distance is obvious, indicative of a declining mass-loss rate. We derive a power-law relationship to fit the maximum mass envelope, which is described by:

$$\max(M_{\text{disk}}) = 0.046 M_{\odot} \left( \frac{d}{0.3 \text{ pc}} \right)^{0.33}. \quad (3)$$

If we assume the disk mass distribution in Orion had no initial dependence on distance, we can estimate how long it would take to photoevaporate it to its present state. The maximum disk mass at  $d \approx 1$  pc is  $0.07 M_{\odot}$ , and at  $d \approx 0.01$  pc is  $0.015 M_{\odot}$ . Assuming a mass loss-rate of  $\dot{M} \sim 10^{-7} M_{\odot} \text{ yr}^{-1}$  at  $d = 0.01$  pc, it would take  $\sim 0.6$  Myrs to truncate the upper end of the disk mass distribution from  $M_{\text{disk}} = 0.07 M_{\odot}$  to  $0.015 M_{\odot}$ , which is consistent with the photoevaporation lifetime of  $\theta^1$  Ori C of  $< 1$  Myr.

We empirically determined the distance,  $d$ , at which the MMSN disk populations within and beyond  $d$  differed with the greatest statistical significance. We found 8/14 disks at  $d > 0.3$  pc have masses  $\geq 0.01 M_{\odot}$ , while only 11/53 disks within 0.3 pc have comparable masses. Fisher’s exact test indicates a 96.2% probability ( $2\sigma$ ) that disks at large and small projected distances from  $\theta^1$  Ori C have different frequencies. This distance represents a statistical boundary for circumstellar disk destruction by external UV photoevaporation in the Orion Nebula Cluster. Orion disks located at  $d < 0.3$  pc have previously been found to have a mass distribution that is truncated at its high end (see Mann & Williams 2009a). Beyond 0.3 pc from  $\theta^1$  Ori C, heating by UV radiation is insufficient to drive appreciable mass-loss in the disks and we find the range in disk masses observed,  $M_{\text{disk}} = 0.004\text{--}0.07 M_{\odot}$ , is similar to the range exhibited by Class II disks in Taurus and  $\rho$  Ophiuchus. We, therefore, expect that Orion disks located beyond 0.3 pc from  $\theta^1$  Ori C evolve similarly to disks in low-mass star forming regions, Taurus and  $\rho$  Ophiuchus, which do not experience UV-driven photoevaporation by nearby massive stars. Furthermore, it is likely that the initial distribution of disk masses in Orion was similar to that observed in Taurus-Auriga and  $\rho$  Ophiuchus, with the Orion disks subsequently photoevaporated from the outside inward, and surviving masses and sizes that are strongly dependent on their stellar masses and distances from  $\theta^1$  Ori C.

#### 4.4. Planet Formation Potential

Despite the clear signs of outer disk destruction observed in Orion, the prospects for inner disk planet formation are not significantly different than in low-mass star forming regions. Overall in Orion, 31% (21/67) of the disks in our sample have masses greater than or equal to the MMSN ( $0.01 M_{\odot}$ ). For comparison, the fraction of Class II disks with masses  $\geq 0.01 M_{\odot}$  in Taurus and  $\rho$ Ophiuchus are  $\sim 37\%$  and  $29\%$ , respectively (Andrews & Williams 2005, 2007a). The fraction of Orion disks with similar properties to the inferred initial conditions of our Solar System, with masses  $\geq 0.01 M_{\odot}$  within 60 AU, is 12/67 ( $\approx 18\%$ ), slightly higher than the percentage found in Taurus-Auriga of  $\approx 13\%$  and comparable to the estimated fraction of stars with gas giant planets within 20 AU (Cumming et al. 2008). Presumably, the lower mass, sub-MMSN disks can form planets less massive than Jupiter, and including these may raise the prospects for planet formation even further. While only a third of the total surveyed disks have masses comparable to a MMSN, all of the disks detected in our survey ( $\approx 57\%$ ) have masses  $\geq 0.28$  MMSN.

### 5. Summary

We have presented the results of our submillimeter interferometric survey of the  $880 \mu\text{m}$  continuum emission from 67 young circumstellar disks in the Orion Nebula Cluster. These observations were taken to study the disk mass distribution in the region, and its dependence on distance from the most massive star of the cluster,  $\theta^1$  Ori C. We find that UV photoevaporation has rapidly ( $< 1$  Myr) eroded the outer parts of the disks located near this massive star, simultaneously reducing their sizes and masses. We present evidence that shows disk masses correlate with distance from  $\theta^1$  Ori C. Circumstellar disk destruction by UV photoevaporation has a statistical limit at the distance of 0.3 pc from  $\theta^1$  Ori C; beyond 0.3 pc, the flux of UV radiation drops and may not adequately heat the disk gas to initiate mass-loss. Despite the hostile environment in the Orion Nebula, the disks appear very similar to those observed in sites of isolated, low-mass star formation, Taurus-Auriga and  $\rho$ Ophiuchus, in that we see:

- Similar disk mass distributions after allowances are made for photoevaporation of the outer disk edges in Orion.
- Grain growth in one Orion disk, 197-427.
- A similar percentage of disks with  $M \geq 0.01 M_{\odot}$  within  $R \leq 60$  AU, which is also comparable to the estimated fraction of radial velocity exoplanets.



We also observed, but did not detect, the largest known disk in Orion, 114-426, due to interference from the strong background molecular cloud emission toward this source. The overall potential to form planets in a rich cluster containing massive stars like Orion is comparable to that found in Taurus-Auriga and  $\rho$ Ophiuchus, a promising result in the search for planets like our own.

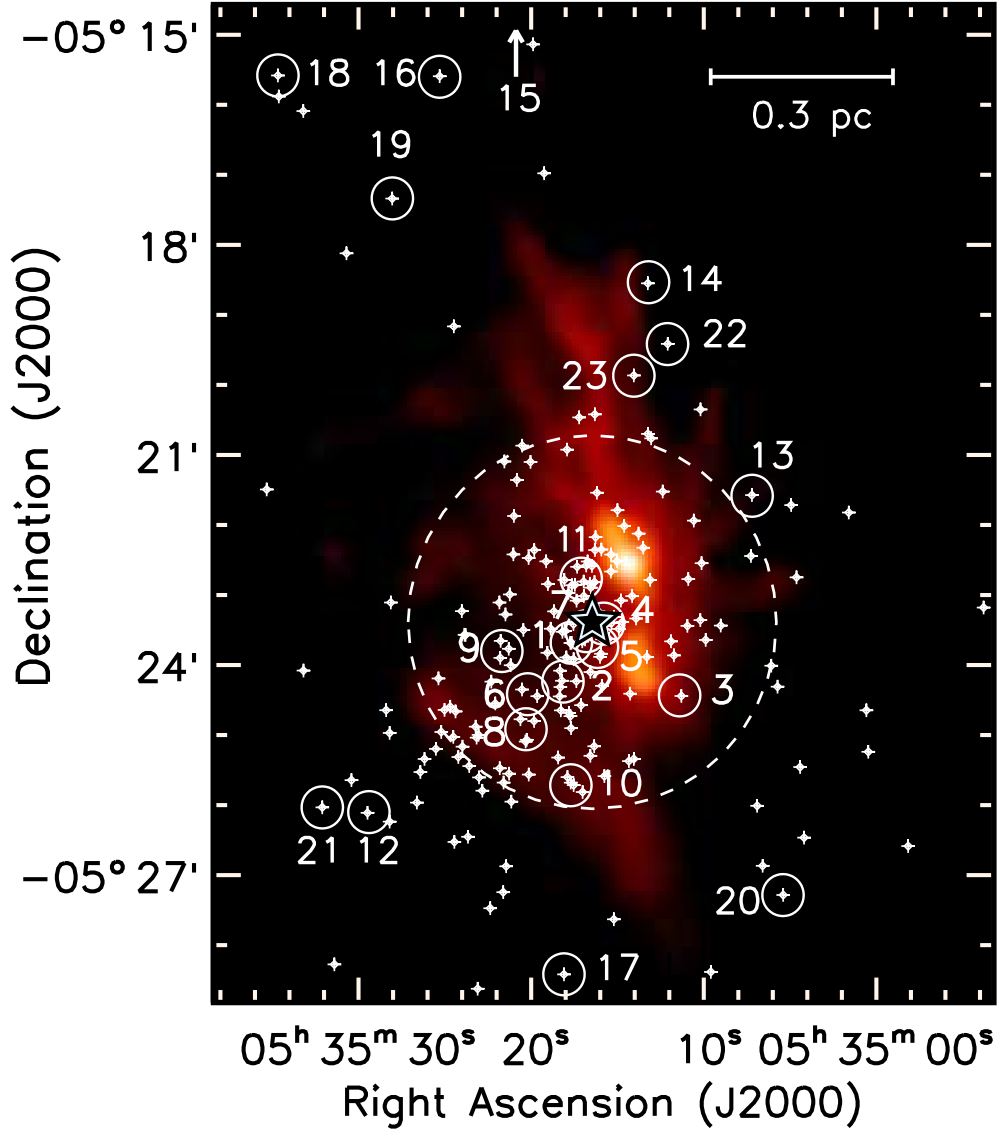


Fig. 1.— Location of the Submillimeter Array (SMA) fields overlaid on a JCMT-SCUBA 850  $\mu\text{m}$  image of Orion. The black and white star near the center of the image marks the position of  $\theta^1$  Ori C of the Trapezium Cluster and white crosses show the location of proplyds identified by HST observations. The solid white circles represent the 32'' primary beam for SMA observations taken at 880  $\mu\text{m}$ . Field numbers are labeled according to Table 1. A dashed circle of radius 0.3 pc, or 155'', around  $\theta^1$  Ori C represents the sphere of influence of the massive star. Field 15, which contains proplyd 216-0939, is located a few arcminutes North of the image.

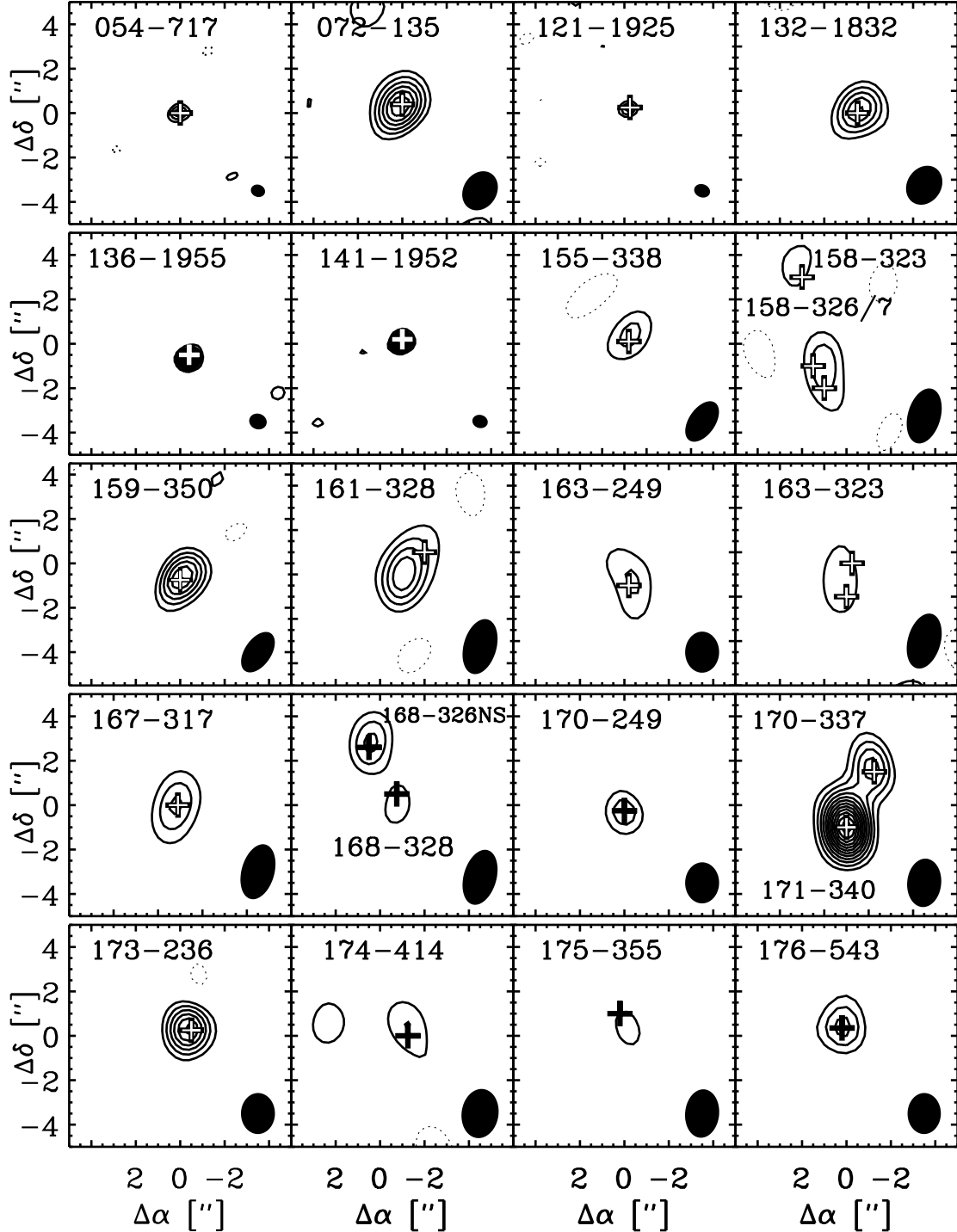


Fig. 2.— Aperture synthesis images of continuum emission at  $880\,\mu\text{m}$  taken with the Submillimeter Array towards proplyds the Orion Nebula Cluster. All proplyds detected at  $\geq 3\sigma$  are shown and labeled with their names (see also Table 2). The positions of the HST-identified proplyds are marked by crosses within the  $10'' \times 10''$  field of view. Contours begin at the  $3\sigma$  level, and each step represents  $2\sigma$  in intensity (see Table 2 for rms noise levels). The synthesized beam is shown in the bottom right corner of each map.

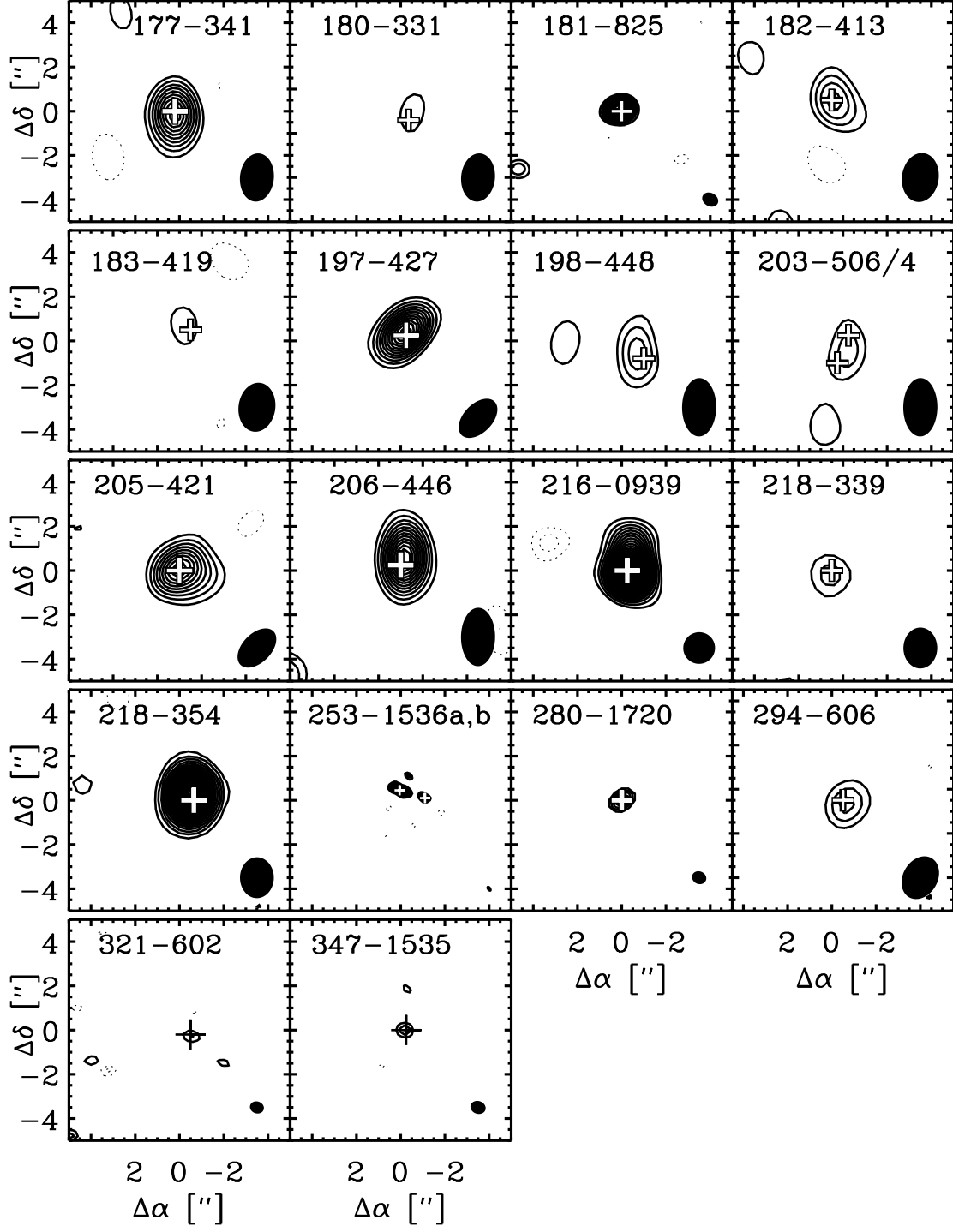


Fig. 3.— Continued from Figure 2.

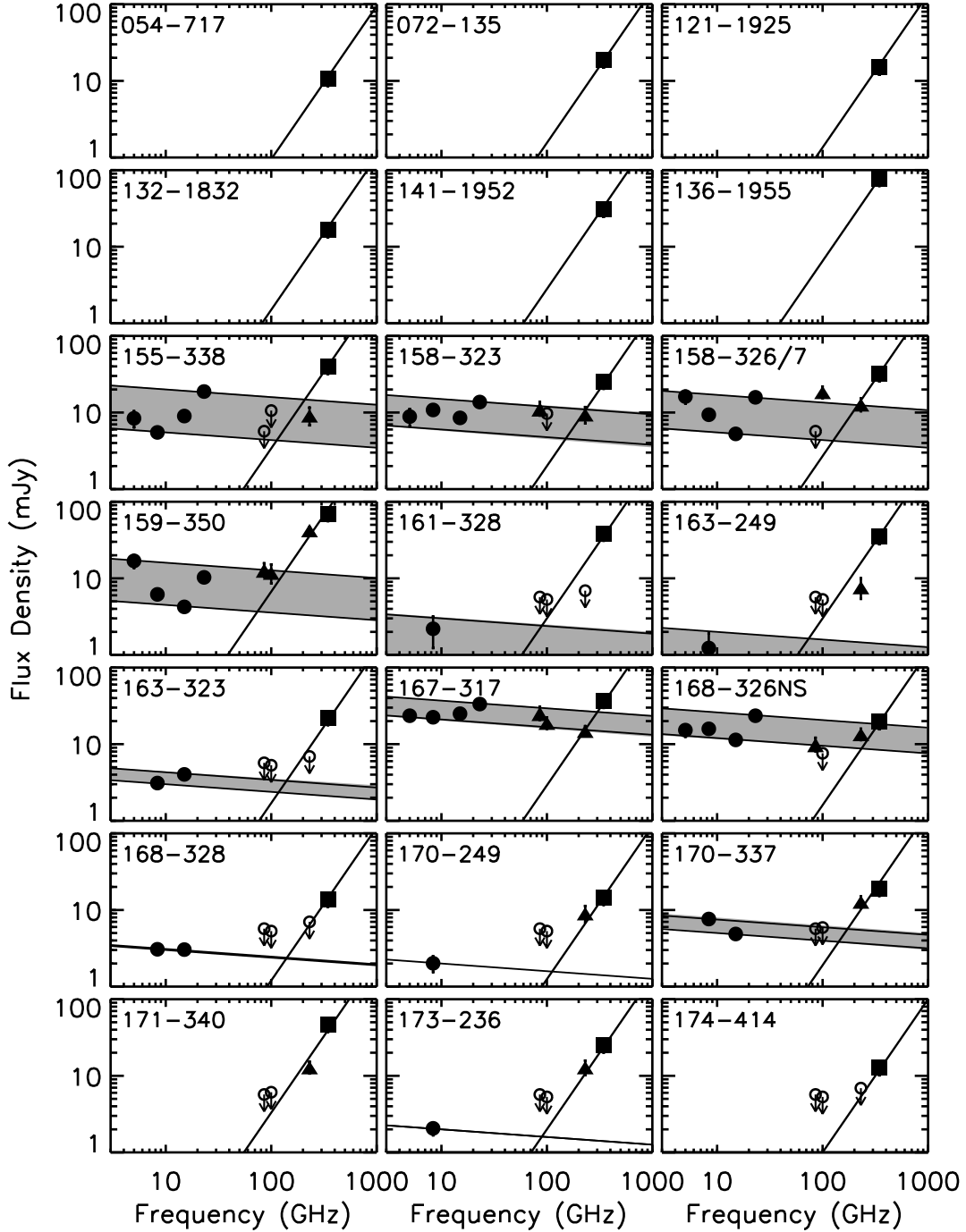


Fig. 4.— Spectral energy distributions for 42 proplyds detected at  $\geq 3\sigma$  with the Submillimeter Array (SMA) at  $880\,\mu\text{m}$ . The SMA measurements are represented by squares, millimeter observations by triangles and centimeter observations by circles. Open circles are upper limits from non-detections and uncertainties not shown are smaller than symbol sizes. The extrapolated range of optically thin free-free emission,  $F_\nu \propto \nu^{-0.1}$ , is overlaid in gray. A template to the disk emission,  $F_\nu \propto \nu^2$ , is shown to guide the eye and reveal the relative contribution of the ionized gas and dust components.

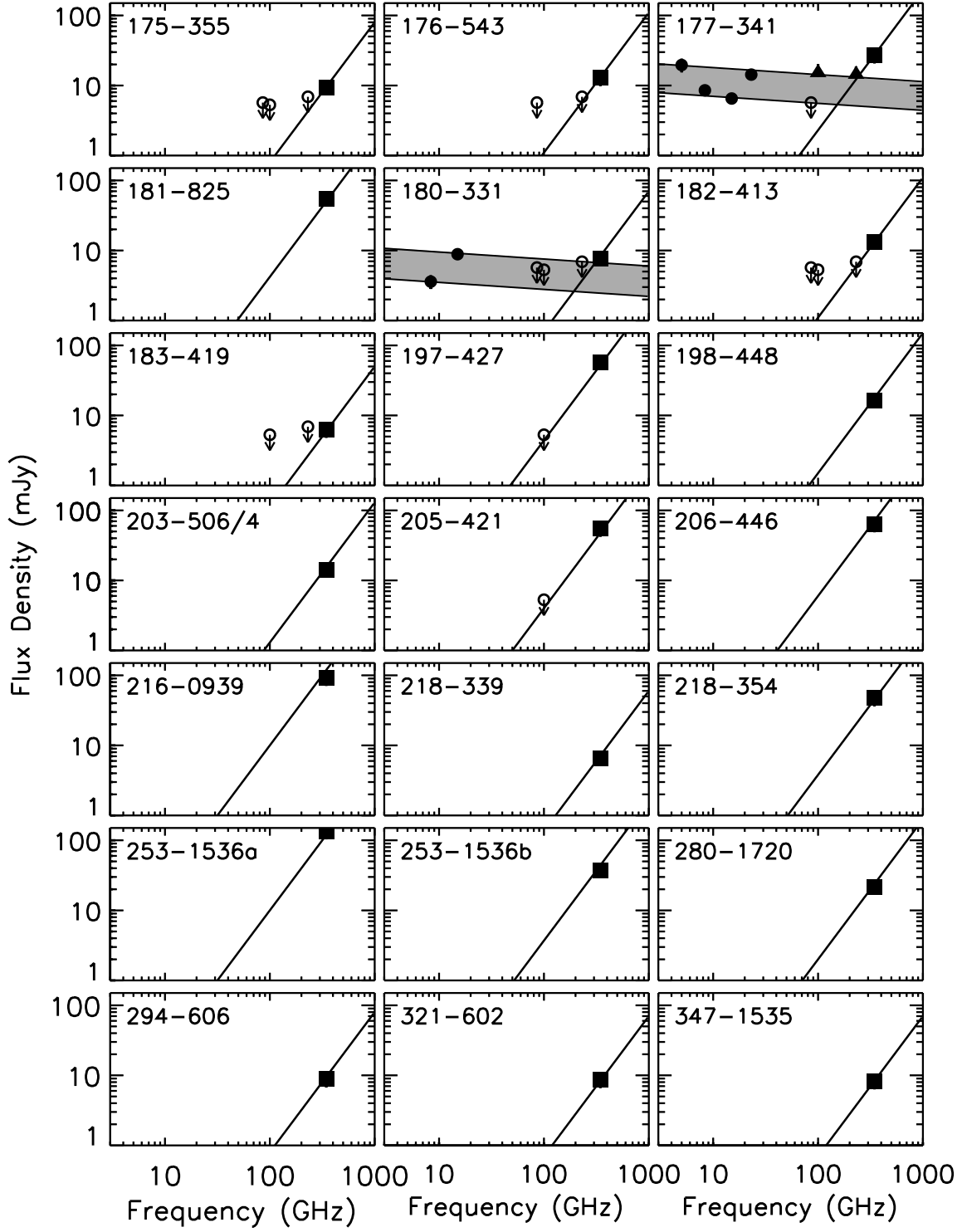


Fig. 5.— Continued from Figure 4.

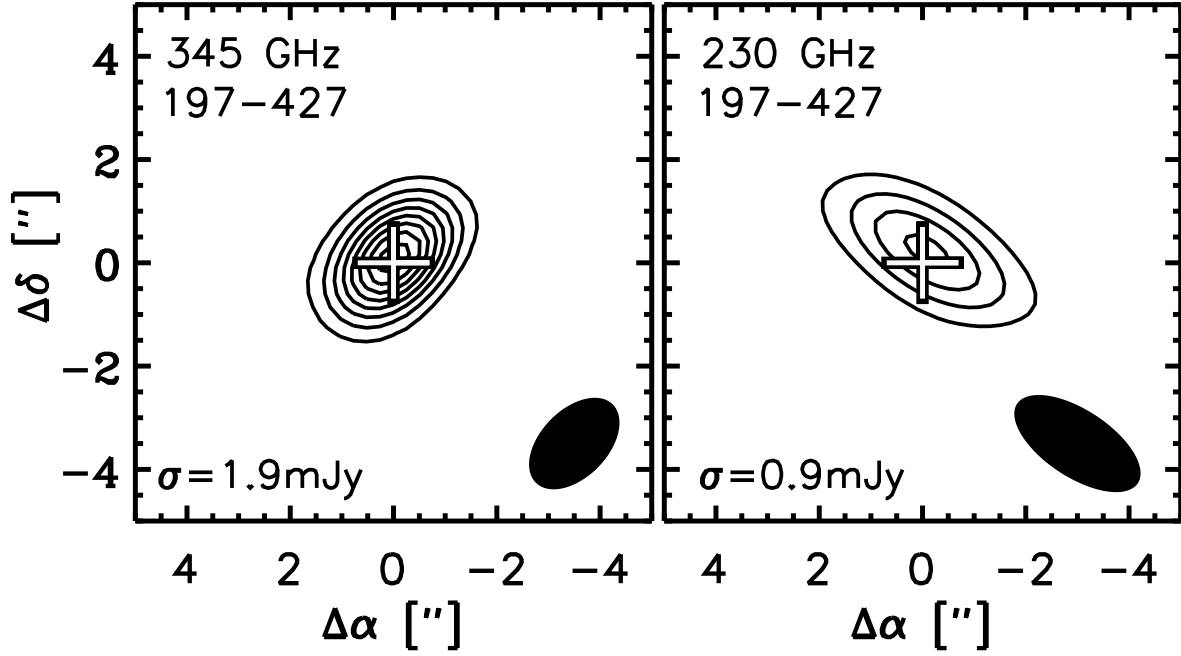


Fig. 6.— Aperture synthesis images of continuum emission at 345 GHz (*left*) and 230 GHz (*right*) taken with the Submillimeter Array towards prominent silhouette disk 197-427 in the Orion Nebula Cluster. The rms noise,  $\sigma$ , is specified in the bottom level corner of each map. The contours shown begin at the  $3\sigma$  level and each contour represents a step of  $2\sigma$  in intensity. The synthesized beam is also shown in the bottom right corner of each map.

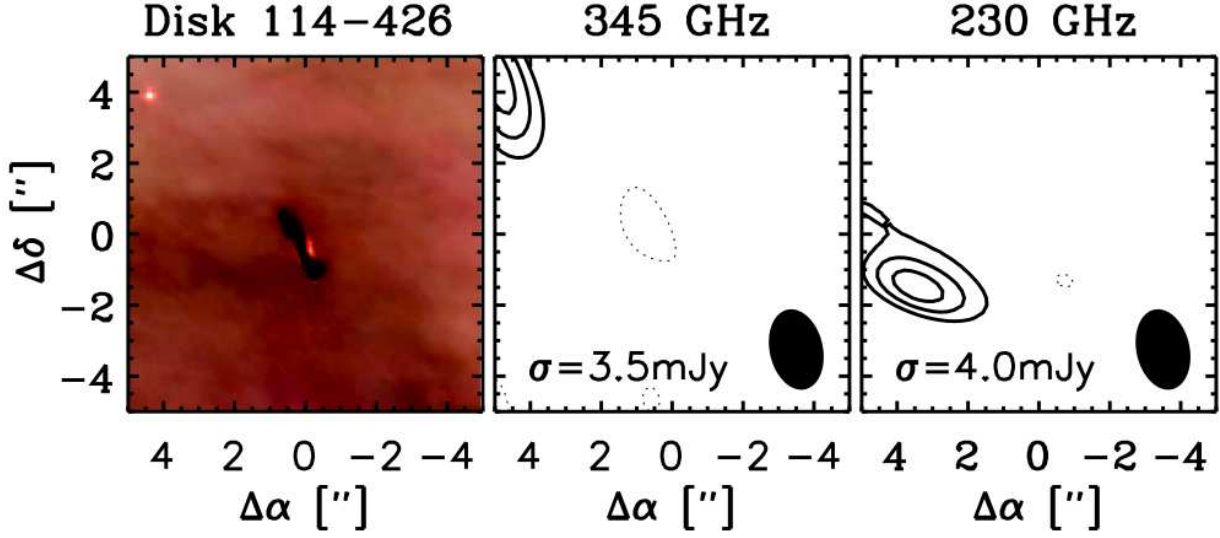


Fig. 7.— Hubble Space Telescope (HST) and Submillimeter Array (SMA) images of disk 114-426 in Orion. At left is an HST image of 114-426 taken from Massimo Robberto. The middle and right panels are aperture synthesis images of continuum emission towards disk 114-426 at 345 GHz (*middle*) and 230 GHz (*right*) and show the disk was not detected at either wavelength. The rms noise,  $\sigma$ , is specified in the lower left corner of the SMA maps. The contours shown begin at the  $2\sigma$  level and each step represents  $1\sigma$  in intensity. The synthesized beam is shown in the bottom right corner of the map.



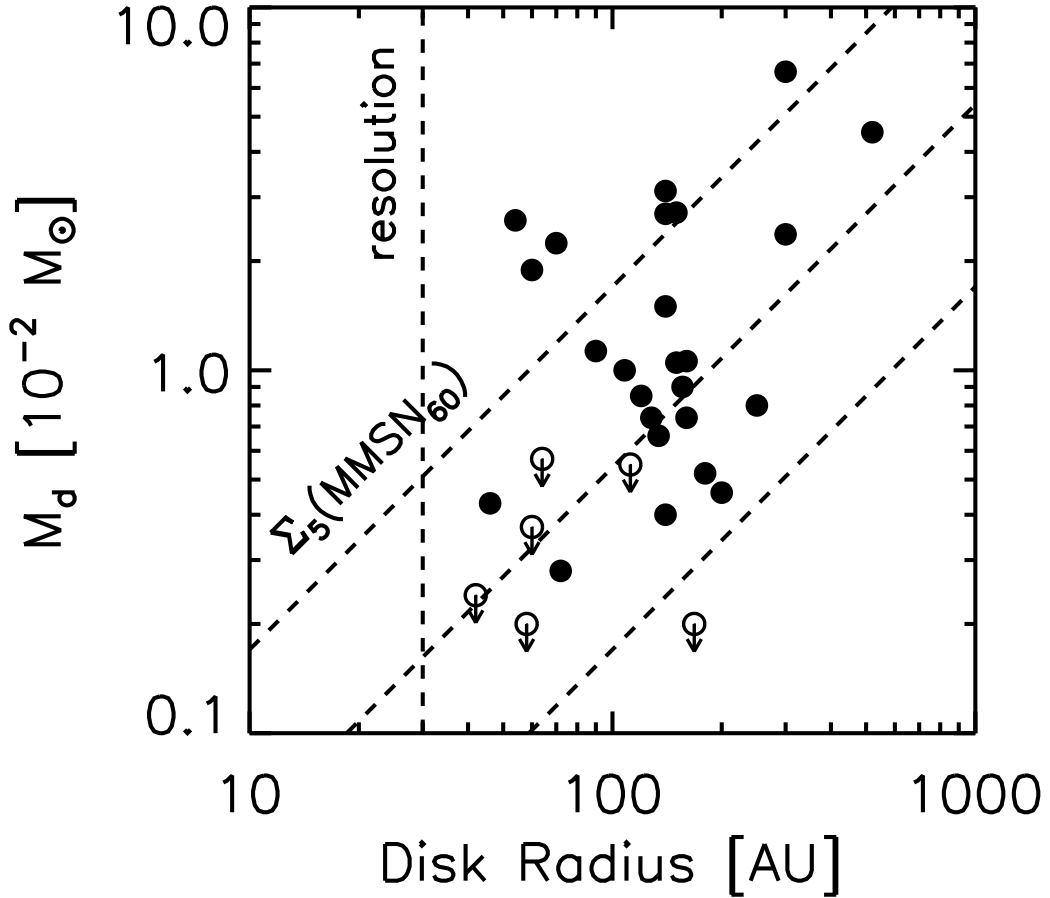


Fig. 8.— Disk masses versus radius for the 31 Orion silhouette disks with resolved sizes from Hubble Space Telescope (HST) imaging. Filled circles represent detections at  $\geq 3\sigma$ , while open circles are the upper limits for the non-detections. The dashed vertical line represents the resolution limit of the HST images,  $0.15'' \approx 60$  AU. The diagonal dashed lines represent different normalizations of the disk surface density, which were calculated assuming  $\Sigma = \Sigma_5 (r/5 \text{ AU})^{-1}$ . The top normalization represents a disk mass of  $0.01 M_\odot$  (MMSN) within 60 AU, and the remaining profiles are a factor of  $\sqrt{10}$  and 10 lower.

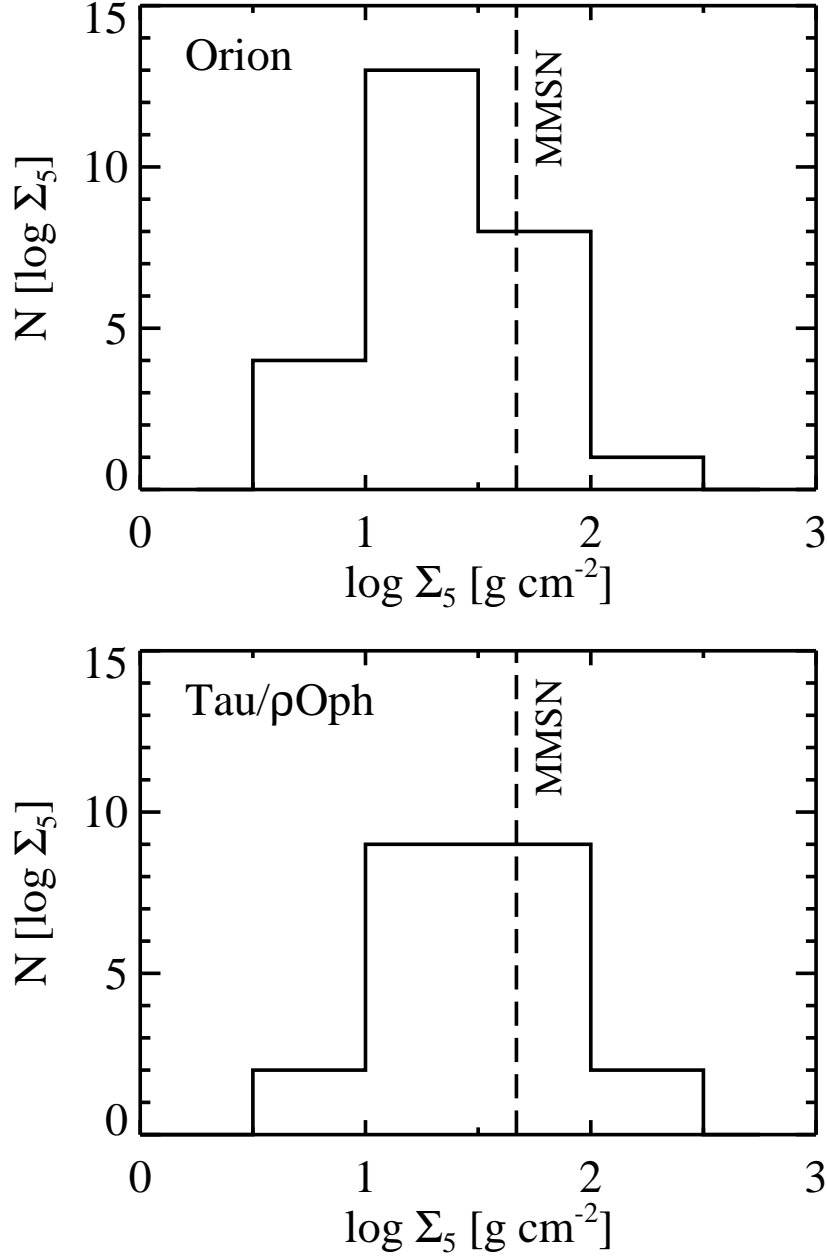


Fig. 9.— The distributions of the normalized disk surface densities at 5 AU,  $\log \Sigma_5$  in Orion (*top*) and Taurus/ $\rho$ Ophiuchus (*bottom*). For Orion, we show the surface densities for the sample of 31 silhouette disks with directly measured sizes from resolved Hubble Space Telescope (HST) images. For the Taurus/ $\rho$ Ophiuchus distribution, the data were taken from Andrews & Williams (2007b). The dashed vertical lines represents the surface density at 5 AU of the MMSN, which was calculated using  $\Sigma = \Sigma_5 (r/5 \text{ AU})^{-1}$ , and shows the majority of disks in both regions have lower surface densities in comparison.

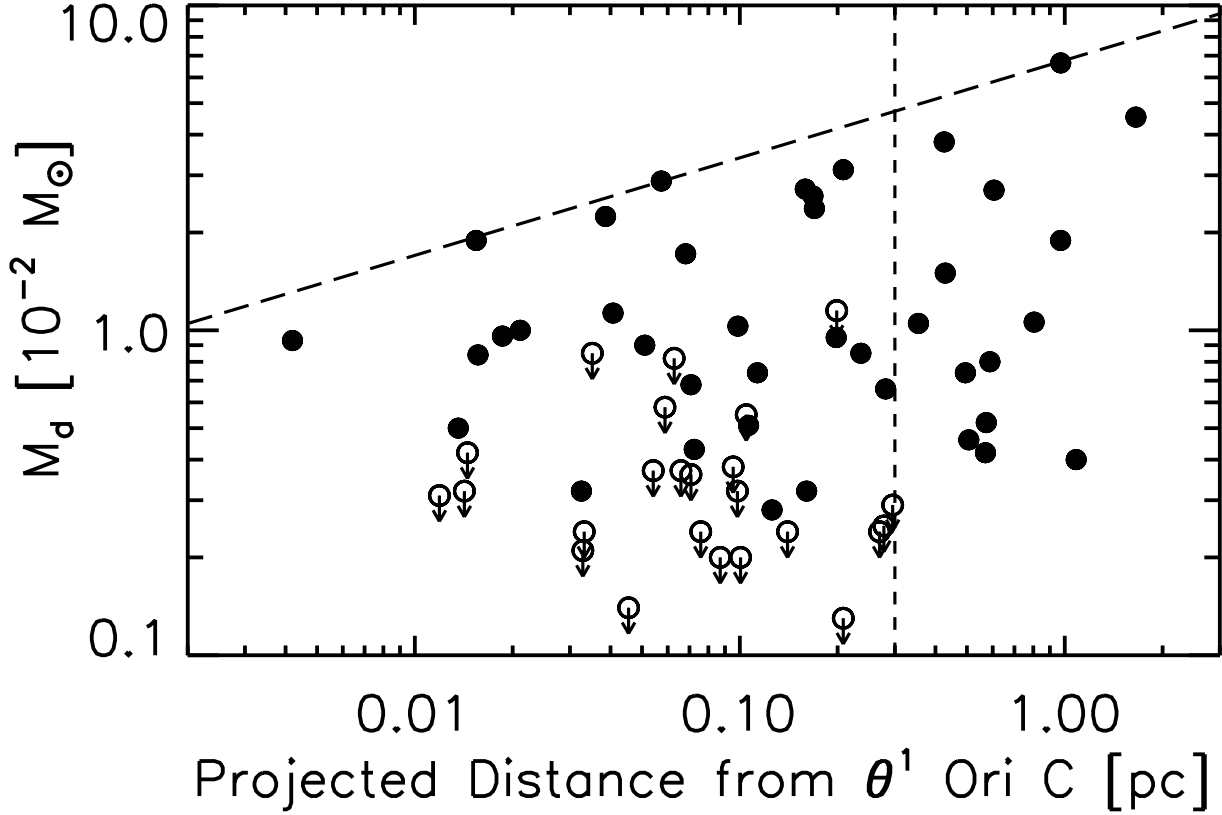


Fig. 10.— Circumstellar disk masses plotted against their projected distances from the massive star,  $\theta^1$  Ori C. Filled circles represent detections, while open circles are the  $3\sigma$  upper limits for the non-detections. The distance of 0.3 pc from  $\theta^1$  Ori C is marked by a dashed line, to separate the statistically different MMSN-populations. The maximum disk mass envelope is traced by the long dashed line across the top, to expose the absence of massive disks near  $\theta^1$  Ori C and the trend of increasing disk mass with distance. A derived power-law fit to the maximum mass envelope follows:  $\max(M_{disk}) = 0.046 M_\odot (d/0.3 \text{ pc})^{0.33}$ .

Table 1. Summary of Submillimeter Array Observations

Field (1)	$\alpha$ (J2000) (2)	$\delta$ (J2000) (3)	$\nu_{LO}$ (GHz) (4)	UT Date (5)	Array (6)	$\tau$ (7)	rms (mJy) (8)	Beam ( $''$ ) (9)	PA( $^\circ$ ) (10)
1 (a)	05 35 17.67	-05 23 40.9	350.175	2006 Dec 27	C	0.03-0.05	1.5	2.3 x 1.6	175.0
2 (c)	05 35 18.16	-05 24 14.2	350.175	2007 Jan 24	C	0.04-0.07	1.6	2.3 x 1.7	169.9
2 (c)	05 35 18.16	-05 24 14.2	224.170	2007 Mar 04	C	0.17-0.23	1.0	2.9 x 1.3	57.5
3	05 35 11.30	-05 24 26.0	224.170	2007 Mar 05	C	0.23-0.25	4.0	2.9 x 1.3	57.0
3	05 35 11.30	-05 24 26.0	340.175	2008 Oct 22	C	0.08-0.09	3.5	2.3 x 1.5	12.6
4	05 35 15.80	-05 23 24.5	349.385	2007 Nov 17	C	0.08-0.1	4.5	1.9 x 1.4	137.4
5 (e)	05 35 20.20	-05 24 25.0	349.379	2007 Nov 25	C	0.06-0.1	1.9	2.2 x 1.4	135.3
6 (d)	05 35 16.16	-05 23 44.5	340.175	2007 Dec 18	C	0.05-0.06	5.8	2.3 x 1.5	145.3
7 (b)	05 35 16.80	-05 23 31.0	340.175	2008 Jan 08	C	0.03-0.04	2.2	2.7 x 1.6	164.2
8 (f)	05 35 20.30	-05 24 55.0	340.175	2008 Mar 14	C	0.09-0.11	2.0	2.6 x 1.5	177.8
9 (h)	05 35 21.70	-05 23 48.0	340.175	2008 Sep 17	C	0.05-0.06	0.7	1.8 x 1.5	1.6
10 (g)	05 35 17.70	-05 25 43.0	340.175	2008 Sep 24	C	0.05-0.15	1.4	2.0 x 1.6	3.0
11 (i)	05 35 17.10	-05 22 46.0	340.175	2008 Sep 30	C	0.05-0.15	2.0	1.8 x 1.5	176.4
12	05 35 29.40	-05 26 06.0	340.175	2008 Nov 11	C	0.06-0.08	1.2	2.2 x 1.8	150.4
13	05 35 07.20	-05 21 35.0	340.175	2008 Nov 26	C	0.08-1.0	1.7	2.1 x 1.6	148.0
14	05 35 13.20	-05 18 32.0	340.175	2008 Dec 21	C	0.06-0.07	1.7	1.9 x 1.5	139.1
15	05 35 21.60	-05 09 39.0	340.175	2008 Dec 23	C	0.10-0.15	1.3	2.1 x 1.6	146.1
16	05 35 25.30	-05 15 36.0	340.175	2008 Dec 24	C	0.13-0.16	2.3	1.9 x 1.4	157.3
16	05 35 25.30	-05 15 36.0	340.175	2009 Mar 26	V	0.05-0.10	1.0	0.3 x 0.2	35.0
16	05 35 25.30	-05 15 36.0	340.175	2009 Mar 27	V	0.03-0.05	1.0	0.3 x 0.2	35.0
17	05 35 18.10	-05 28 25.0	340.175	2009 Aug 25	E	0.04-0.06	1.0	0.9 x 0.7	110.1
18	05 35 34.67	-05 15 34.7	340.765	2010 Jan 19	E	0.02-0.03	1.4	0.7 x 0.6	110.0
19	05 35 28.04	-05 17 20.0	340.765	2010 Jan 19	E	0.02-0.03	0.7	0.8 x 0.6	122.6
20	05 35 05.40	-05 27 17.1	342.000	2010 Feb 28	E	0.06-0.08	1.4	0.8 x 0.7	106.6
21	05 35 32.10	-05 26 02.0	342.000	2010 Feb 28	E	0.06-0.08	1.5	0.7 x 0.5	97.8
22	05 35 12.10	-05 19 25.0	340.765	2010 Feb 29	E	0.05-0.08	1.5	0.7 x 0.6	109.9
23	05 35 14.05	-05 19 52.1	340.765	2010 Feb 29	E	0.05-0.08	1.2	0.8 x 0.7	69.7

Note. — NOTES — Column 1: Field Number; also labeled in Figure 1. Previous designation from (Mann & Williams 2009b) listed in brackets. Column 2, 3: Phase Center Coordinates. Column 4: Observing Frequency. Column 5: UT Date of Observation. Column 6: Array configuration; C, compact (16-70 m baselines), E, extended (28-226 m baselines), V, very extended (68-509 m baselines). Column 7: Zenith optical depth at 225 GHz. Column 8: Root mean square noise measured in emission-free regions within the primary beam. Column 9: Dimensions of the naturally weighted synthesized beam. Column 10: Position angle of synthesized beam, measured east of north.

Table 2. Disk Fluxes and Masses

Proplyd	Field	F <sub>obs</sub> [mJy]	rms [mJy]	F <sub>ff</sub> [mJy]	F <sub>bg</sub> [mJy]	F <sub>dust</sub> [mJy]	M <sub>disk</sub> [0.01M <sub>⊙</sub> ]
(1)	(2)	(3)	(4)	(5)	(6)	(7)	(8)
054-717	20	10.7	1.4	0.0	0.0	10.7	0.52 ± 0.07
072-135	13	18.6	1.7	0.0	-2.8	11.5	1.05 ± 0.08
121-1925	22	15.0	1.5	0.0	0.0	15.0	0.74 ± 0.07
132-1832	14	16.5	1.7	0.0	0.2	16.3	0.80 ± 0.08
136-1955	23	77.6	1.2	0.0	0.0	77.6	3.80 ± 0.07
141-1952	23	30.6	1.2	0.0	0.0	30.6	1.50 ± 0.06
155-338	5	39.6	5.3	4.0–14.0	2.6	23.0	1.13 ± 0.34
158-323	7	25.4	2.4	4.3–11.5	-5.6	19.5	0.96 ± 0.21
158-326/7	7	31.9	2.4	4.0–12.0	-0.5	20.3	1.00 ± 0.19
159-350	5	69.8	5.3	3.2–11.0	0.3	58.4	2.88 ± 0.29
161-328	7	38.7	2.4	0.1–1.5	-1.2	38.4	1.89 ± 0.15
163-249	11	34.8	2.0	0.0	-1.6	35.0	1.72 ± 0.13
163-323	7	22.1	2.4	2.4–3.0	0.2	18.9	0.93 ± 0.15
167-317	7	37.2	2.4	14.5–25.5	-5.4	17.0	0.84 ± 0.18
168-328	7	13.7	2.4	1.9–2.5	1.0	10.3	0.50 ± 0.12
170-249	11	14.6	2.0	0.0–2.5	-0.6	13.7	0.68 ± 0.10
170-337	1	19.1	1.5	4.0–9.0	3.0	7.1	0.32 ± 0.08
171-340	1	46.4	1.5	0.0	-2.8	49.2	2.24 ± 0.08
173-236	1	25.2	2.0	0.0	2.9	20.8	1.03 ± 0.13
174-414	2	12.7	1.5	0.0	1.6	11.1	0.51 ± 0.09
175-355	8	9.4	1.5	0.0	-0.1	9.5	0.43 ± 0.11
176-543	10	12.8	1.4	0.0	-0.6	13.4	0.66 ± 0.07
177-341	1	26.9	1.5	5.0–13.0	-5.9	19.8	0.90 ± 0.07
181-825	17	54.8	1.0	0.0	0.0	54.8	2.70 ± 0.05
182-413	2	13.3	1.5	0.0	-3.0	16.4	0.74 ± 0.07
183-419	2	6.2	1.5	0.0	0.2	6.1	0.28 ± 0.07
197-427	6	57.7	1.9	0.0	-1.5	59.3	2.72 ± 0.10
198-448	8	16.4	2.0	0.0	-2.9	19.3	0.95 ± 0.12
203-506/4	8	14.3	2.0	0.0	-2.9	17.2	0.85 ± 0.13
205-421	6	54.8	1.9	0.0	-1.7	56.5	2.59 ± 0.10
206-446	8	63.2	2.0	0.0	0.0	63.3	3.12 ± 0.12
216-0939	15	91.9	1.3	0.0	0.0	91.9	4.53 ± 0.06
218-339	9	6.6	0.7	0.0	0.0	6.6	0.32 ± 0.04
218-354	9	42.3	0.7	0.0	-0.9	48.1	2.37 ± 0.04
253-1536a	16	134.2	1.0	0.0	-0.8	135.0	6.65 ± 0.05
253-1536b	16	37.6	1.0	0.0	-0.8	38.4	1.89 ± 0.05
280-1720	19	21.8	0.7	0.0	0.0	21.8	1.06 ± 0.03
294-606	12	8.8	1.2	0.0	-0.5	9.3	0.46 ± 0.06
321-602	21	8.6	1.5	0.0	0.0	8.6	0.42 ± 0.07
347-1535	18	8.2	1.4	0.0	0.0	8.2	0.40 ± 0.07

Note. — NOTES — Column 1: Proplyd designation based on the nomenclature of O’Dell & Wen (1994). Column 2: Observed Field in Figure 1 and Table 1. Column 3: Integrated continuum flux density, corrected for SMA primary beam attenuation. Column 4:  $1\sigma$  statistical error. Column 5: Range of extrapolated contribution of

free-free emission at  $880\,\mu\text{m}$ . Column 6: Estimated flux contribution from cloud background. Column 7: Derived dust continuum flux from the disk. Column 8: Disk mass (error does not include uncertainties in the flux scale of  $\sim 15\%$ ).

Table 3. Upper Limits on Disk Fluxes and Masses

Proplyd	Field	$3\sigma$ [mJy]	$F_{\text{ff}}$ [mJy]	$F_{\text{bg}}$ [mJy]	$M_{\text{disk}}$ [ $0.01M_{\odot}$ ]
(1)	(2)	(3)	(4)	(5)	(6)
114-426	3	< 10.5	0	-12.8	< 1.15
159-338	6	< 17.4	0.0–1.2	-0.9	< 0.85
160-353	6	< 19.3	0.0–2.0	0.5	< 0.82
161-324	7	< 10.0	2.5–4.5	-0.8	< 0.31
163-317	7	< 12.8	4.6–12.0	-5.7	< 0.32
165-235	11	< 9.3	0	1.6	< 0.38
165-254	11	< 8.0	0	-3.7	< 0.57
166-250	11	< 7.1	0	-0.3	< 0.37
166-316	7	< 11.6	0.1–1.5	1.7	< 0.42
167-231	11	< 10.5	0	-0.6	< 0.55
168-235	11	< 8.4	0	2.0	< 0.32
168-326NS	7	19.6	8.6–18.0	1.2	< 0.02
169-338	1	< 6.0	0	0.7	< 0.24
169-549	10	< 4.6	0	-1.3	< 0.29
171-334	1	< 5.7	1.9–4.7	1.2	< 0.07
173-341	1	< 4.6	0	1.6	< 0.14
175-251	11	< 6.7	0	-0.5	< 0.36
176-325	7	< 10.2	2.8–4.0	1.9	< 0.21
177-541	10	< 4.3	0	-0.8	< 0.25
179-353	1	< 6.5	0	1.3	< 0.24
179-534	10	< 4.7	0	-0.2	< 0.24
180-331	1	7.7	2.1–6.7	2.1	< 0.07
181-247	11	< 9.3	1.6–3.2	0.9	< 0.20
182-332	1	< 6.1	0	-2.1	< 0.37
183-405	2	< 5.9	0	1.5	< 0.20
184-427	2	< 7.0	0	1.7	< 0.24
213-346	9	< 2.6	0	0.0	< 0.13

Note. — NOTES — Column 1: Proplyd designation based on the nomenclature of O’Dell & Wen (1994). Column 2: Observed Field in Figure 1 and Table 1. Column 3:  $3\sigma$  flux upper limits (or integrated continuum flux density for 168-326N, 180-331), corrected for primary beam attenuation. Column 4: Extrapolated contribution of free-free emission at  $880\mu\text{m}$ . Column 5: Estimated flux contribution from cloud background at  $880\mu\text{m}$ . Column 6:  $3\sigma$  disk mass upper limit.

Table 4. Submillimeter Continuum Slopes

Proplyd	Field	$F_{880\mu\text{m}}$ [mJy]	$F_{1330\mu\text{m}}$ [mJy]	$\alpha$
(1)	(2)	(3)	(4)	(5)
197-427	2	57.7	17.4	$2.8 \pm 0.1$
174-414	2	12.7	<3.4	$> 3.0 \pm 0.1$
182-413	2	13.3	<3.0	$> 3.4 \pm 0.1$
183-419	2	6.2	<3.1	$> 1.6 \pm 0.1$
114-426	3	<10.5	<12.0	

Note. — NOTES — Column 1: Proplyd designation based on the nomenclature of O’Dell & Wen (1994). Column 2: Observed Field in Figure 1. Column 3: Integrated continuum flux density at  $880\mu\text{m}$ , corrected for primary beam attenuation. Column 4: Integrated continuum flux density at  $1330\mu\text{m}$ , corrected for primary beam attenuation. Column 5: Submillimeter SED Slope as defined in Section 3.4. comparison of SMA and CARMA observations.

Table 5. Statistical Correlation Tests of Orion Disk Properties

Correlaton Test	Mass vs. Size P(%)	Mass vs. Distance P(%)
(1)	(2)	(3)
Cox Hazard	99.95 ( $3.5\sigma$ )	99.99 ( $4.0\sigma$ )
Kendall’s $\tau$	95.36 ( $2.0\sigma$ )	98.74 ( $2.5\sigma$ )
Spearman’s $\rho$	97.17 ( $2.2\sigma$ )	99.07 ( $2.6\sigma$ )

Note. — NOTES — Column 1: Censored statistical correlation tests were used that incorporate  $3\sigma$  upper limits for the non-detections (Isobe et al. 1986). These tests include the Cox Proportional Hazard Model, the Generalized Kendall’s  $\tau$ , and Spearman’s  $\rho$ . Column 2: Probability of correlation between disk size and mass for silhouette disks. Column 3: Probability of correlation between disk mass and the projected distance of the disk from  $\theta^1$  Ori C.



## REFERENCES

- Adams, F. C., Hollenbach, D., Laughlin, G., & Gorti, U. 2004, *ApJ*, 611, 360
- Andre, P. & Montmerle, T. 1994, *ApJ*, 420, 837
- Andrews, S. M. & Williams, J. P. 2005, *ApJ*, 631, 1134
- . 2007a, *ApJ*, 671, 1800
- . 2007b, *ApJ*, 659, 705
- Andrews, S. M., Wilner, D. J., Hughes, A. M., Qi, C., & Dullemond, C. P. 2009, *ApJ*, 700, 1502
- Bally, J., O’Dell, C. R., & McCaughrean, M. J. 2000, *AJ*, 119, 2919
- Bally, J., Sutherland, R. S., Devine, D., & Johnstone, D. 1998a, *AJ*, 116, 293
- Bally, J., Testi, L., Sargent, A., & Carlstrom, J. 1998b, *AJ*, 116, 854
- Beckwith, S. V. W. & Sargent, A. I. 1991, *ApJ*, 381, 250
- Beckwith, S. V. W., Sargent, A. I., Chini, R. S., & Guesten, R. 1990, *AJ*, 99, 924
- Birnstiel, T., Dullemond, C. P., & Brauer, F. 2009, *A&A*, 503, L5
- Bonnell, I. A., Bate, M. R., & Vine, S. G. 2003, *MNRAS*, 343, 413
- Churchwell, E., Felli, M., Wood, D. O. S., & Massi, M. 1987, *ApJ*, 321, 516
- Clarke, C. J. 2007, *MNRAS*, 376, 1350
- Cumming, A., Butler, R. P., Marcy, G. W., Vogt, S. S., Wright, J. T., & Fischer, D. A. 2008, *PASP*, 120, 531
- D’Alessio, P., Calvet, N., & Hartmann, L. 2001, *ApJ*, 553, 321
- Dullemond, C. P. & Dominik, C. 2005, *A&A*, 434, 971
- Eisner, J. A. & Carpenter, J. M. 2006, *ApJ*, 641, 1162
- Eisner, J. A., Plambeck, R. L., Carpenter, J. M., Corder, S. A., Qi, C., & Wilner, D. 2008, *ApJ*, 683, 304
- Evans, II, N. J. 1999, *ARA&A*, 37, 311

- Felli, M., Churchwell, E., Wilson, T. L., & Taylor, G. B. 1993, *A&AS*, 98, 137
- Gaidos, E., Krot, A. N., Williams, J. P., & Raymond, S. N. 2009, *ApJ*, 696, 1854
- Garay, G., Moran, J. M., & Reid, M. J. 1987, *ApJ*, 314, 535
- Hartmann, L., Calvet, N., Gullbring, E., & D’Alessio, P. 1998, *ApJ*, 495, 385
- Henney, W. J. & O’Dell, C. R. 1999, *AJ*, 118, 2350
- Hillenbrand, L. A. 1997, *AJ*, 113, 1733
- Hillenbrand, L. A. & Carpenter, J. M. 2000, *ApJ*, 540, 236
- Ho, P. T. P., Moran, J. M., & Lo, K. Y. 2004, *ApJ*, 616, L1
- Isobe, T., Feigelson, E. D., & Nelson, P. I. 1986, *ApJ*, 306, 490
- Johnstone, D. & Bally, J. 1999, *ApJ*, 510, L49
- . 2006, *ApJ*, 653, 383
- Johnstone, D., Fich, M., Mitchell, G. F., & Moriarty-Schieven, G. 2001, *ApJ*, 559, 307
- Johnstone, D., Hollenbach, D., & Bally, J. 1998, *ApJ*, 499, 758
- Johnstone, D., Matthews, H., & Mitchell, G. F. 2006, *ApJ*, 639, 259
- Kraus, S., Balega, Y. Y., Berger, J., Hofmann, K., Millan-Gabet, R., Monnier, J. D., Ohnaka, K., Pedretti, E., Preibisch, T., Schertl, D., Schloerb, F. P., Traub, W. A., & Weigelt, G. 2007, *A&A*, 466, 649
- Kraus, S., Weigelt, G., Balega, Y. Y., Docobo, J. A., Hofmann, K., Preibisch, T., Schertl, D., Tamazian, V. S., Driebe, T., Ohnaka, K., Petrov, R., Schöller, M., & Smith, M. 2009, *A&A*, 497, 195
- Krot, A. N., Scott, E. R. D., & Reipurth, B., eds. 2005, *Astronomical Society of the Pacific Conference Series*, Vol. 341, *Chondrites and the Protoplanetary Disk*
- Lada, C. J. & Lada, E. A. 2003, *ARA&A*, 41, 57
- Laques, P. & Vidal, J. L. 1979, *A&A*, 73, 97
- Mann, R. K. & Williams, J. P. 2009a, *ApJ*, 699, L55
- . 2009b, *ApJ*, 694, L36

- Matsuyama, I., Johnstone, D., & Hartmann, L. 2003, *ApJ*, 582, 893
- McCaughrean, M. J., Chen, H., Bally, J., Erickson, E., Thompson, R., Rieke, M., Schneider, G., Stolovy, S., & Young, E. 1998, *ApJ*, 492, L157+
- McCaughrean, M. J. & O’dell, C. R. 1996, *AJ*, 111, 1977
- McCullough, P. R., Fugate, R. Q., Christou, J. C., Ellerbroek, B. L., Higgins, C. H., Spinhirne, J. M., Cleis, R. A., & Moroney, J. F. 1995, *ApJ*, 438, 394
- Menten, K. M., Reid, M. J., Forbrich, J., & Brunthaler, A. 2007, *A&A*, 474, 515
- Moran, J. M., Garay, G., Reid, M. J., Genzel, R., & Ho, P. T. P. 1982, *New York Academy Sciences Annals*, 395, 204
- Mundy, L. G., Looney, L. W., & Lada, E. A. 1995, *ApJ*, 452, L137+
- O’dell, C. R. & Wen, Z. 1994, *ApJ*, 436, 194
- O’dell, C. R., Wen, Z., & Hu, X. 1993, *ApJ*, 410, 696
- O’dell, C. R. & Wong, K. 1996, *AJ*, 111, 846
- Osterloh, M. & Beckwith, S. V. W. 1995, *ApJ*, 439, 288
- Parravano, A., Hollenbach, D. J., & McKee, C. F. 2003, *ApJ*, 584, 797
- Pollack, J. B., Hollenbach, D., Beckwith, S., Simonelli, D. P., Roush, T., & Fong, W. 1994, *ApJ*, 421, 615
- Ricci, L., Robberto, M., & Soderblom, D. R. 2008, *AJ*, 136, 2136
- Ricci, L., Testi, L., Natta, A., Neri, R., Cabrit, S., & Herczeg, G. J. 2010, *A&A*, 512, A15+
- Richling, S. & Yorke, H. W. 2000, *ApJ*, 539, 258
- Rodmann, J., Henning, T., Chandler, C. J., Mundy, L. G., & Wilner, D. J. 2006, *A&A*, 446, 211
- Sandstrom, K. M., Peek, J. E. G., Bower, G. C., Bolatto, A. D., & Plambeck, R. L. 2007, *ApJ*, 667, 1161
- Sault, R. J., Teuben, P. J., & Wright, M. C. H. 1995, in *Astronomical Society of the Pacific Conference Series*, Vol. 77, *Astronomical Data Analysis Software and Systems IV*, ed. R. A. Shaw, H. E. Payne, & J. J. E. Hayes, 433–+

- Scally, A. & Clarke, C. 2001, MNRAS, 325, 449
- Shuping, R. Y., Bally, J., Morris, M., & Throop, H. 2003, ApJ, 587, L109
- Smith, N., Bally, J., Licht, D., & Walawender, J. 2005, AJ, 129, 382
- Störzer, H. & Hollenbach, D. 1999, ApJ, 515, 669
- Tachibana, S., Huss, G. R., Kita, N. T., Shimoda, G., & Morishita, Y. 2006, ApJ, 639, L87
- Throop, H. B., Bally, J., Esposito, L. W., & McCaughrean, M. J. 2001, Science, 292, 1686
- Vicente, S. M. & Alves, J. 2005, A&A, 441, 195
- Weidenschilling, S. J. 1977, Ap&SS, 51, 153
- Williams, J. P., Andrews, S. M., & Wilner, D. J. 2005, ApJ, 634, 495
- Wilner, D. J., D’Alessio, P., Calvet, N., Claussen, M. J., & Hartmann, L. 2005, ApJ, 626, L109
- Zapata, L. A., Rodríguez, L. F., Kurtz, S. E., & O’Dell, C. R. 2004, AJ, 127, 2252